Results from parallel observations of superconducting and absolute gravimeters and GPS at the Hsinchu station of Global Geodynamics Project, Taiwan

Cheinway Hwang,[1] Ricky Kao,[1,2] Ching-Chung Cheng,[1] Jiu-Fu Huang,[1,3] Chiung-Wu Lee,[2] and Tadahiro Sato[4]

[1]   The Hsinchu (HS) superconducting gravimeter (SG, serial T48) station is a newly established site in the Global Geodynamics Project (GGP). Simultaneous observations of T48, three FG5 absolute gravimeters, and GPS at four stations are studied. GPS shows few mm a^{-1} of horizontal and vertical motions around HS. The calibration factor and drifting rate of T48 are $-75.96 \pm 0.07 \ \mu\text{Gal V}^{-1}$ and $0.2 \pm 0.7 \ \mu\text{Gal a}^{-1}$ ($1 \ \mu\text{Gal} = 10^{-8} \text{ m s}^{-2}$). Both the SG and absolute gravity records contain trends of about $2-3 \ \mu\text{Gal a}^{-1}$. The ocean tide gravity effects (OTGEs) were estimated from NAO.99b, FES2004, and CSR4.0, and their amplitudes agree with the SG observations at the submicroGal level, but their phases differ from the observations up to $10°$. The Newtonian effect of ocean tide contributes 20% to the total OTGE at HS, and it is larger at islands in the Taiwan Strait. The inelastic body tide model of Dehant et al. (1999) is more consistent with the SG observations than the elastic model. Modeled gravity-atmosphere admittances based on an exponential distribution of air mass explain well the observed admittances. The average gravity-atmosphere admittance during typhoons is 30% larger than that in a nontyphoon time. A list of coseismic gravity changes from T48 caused by earthquakes over 2006–2007 is given for potential studies of fault parameters. The modeled effects of atmospheric pressure, groundwater, soil moisture, and polar motion explain the FG5 observed gravity trend to $1.1 \ \mu\text{Gal a}^{-1}$. Seasonally, the groundwater-induced gravity change contributes the most to the SG residual gravity, but its phase leads the latter by 63 days.

1.   Introduction

[2]   In March 2006, a single-sphere superconducting gravimeter (SG), serial number T48, was installed at Tunnel B of Mt. 18-Peak in the Hsinchu City, Taiwan. T48 is manufactured by GWR and has a nominal sensitivity of 1 nGal and a stability of few $\mu\text{Gal a}^{-1}$ or better (1 nGal = 10^{-11} m s^{-2}; 1 μGal = 10^{-8} m s^{-2}). The Hsinchu SG station is now included in the SG network of the Global Geodynamics Project (GGP, http://www.eas.slu.edu/GGP/ggphome.html). The latitude, longitude and elevation of HS are 24.79258°N and 120.98554°E and 87.6 m, respectively.

The scientific objectives and related issues of GGP, in particular GGP's role in the Global Geodetic Observing System (GGOS), are detailed by *Hinderer and Crossley* [2004] and *Forsberg et al.* [2005], and will not be elaborated here. Hereafter we will use the abbreviation HS to represent the Hsinchu SG station. Also, a second SG–T49 at HS is under test, but its result will not be reported here. Several meteorological sensors, a seismometer, a continuous GPS station and a groundwater monitoring well are deployed to monitor environment-induced gravity changes. Also, HS is about 8.6 km from the Taiwan Strait, where the average depth is 80 m and the ocean tide amplitude and phase are rapidly varying [*Jan et al.*, 2004]. Taiwan, like many other regions in the western Pacific, is prone to attacks from such hazards as landslide, typhoon and earthquake. Installed at a proper location, a SG may be used to monitor man-made and natural hazards.

[3]   In addition to supplying SG data to users interested in the targeted research subjects listed in GGP and GGOS, HS offers some extra features. HS is the closest station to the Tropic of Cancer in GGP and will be most sensitive to

---
[1]Department of Civil Engineering, National Chiao Tung University, Hsinchu, Taiwan.
[2]Dimensional Measurement Laboratory, Measurement Standards and Technology Division, CMS, ITRI, Hsinchu, Taiwan.
[3]Ministry of Interior, Taipei, Taiwan.
[4]Research Center for Prediction of Earthquakes and Volcanic Eruptions, Tohoku University, Sendai, Japan.
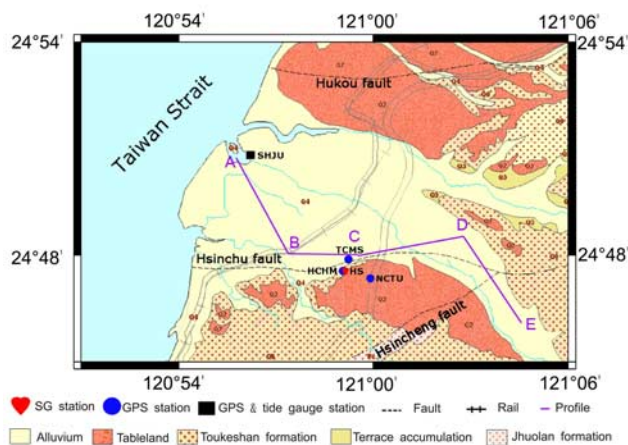
Figure 1. Geological settings around the Hsinchu (HS) superconducting gravimeter (SG) station, and distributions of GPS and tide gauge stations. The meanings of the formations are explained by documents in the Central Geological Survey of Taiwan (http://www.moeacgs. gov.tw).

gravity change owing to the motion of the Earth's inner core in the summer solstice, so that the SG data here are the best for testing the universality of free fall [*Shiomi*, 2006]. Because of the short distance to shallow waters (8.6 km to the Taiwan Strait in the west), and the medium distance to deep waters (about 100 km to the Pacific in the east), the SG data at HS can be useful for studying the Newtonian effect and the loading effect of ocean tide. SG data at HS will enable the detection of nonlinear ocean tides originating from the Taiwan Strait [*Boy et al.*, 2004; *Khan and Høyer*, 2004]. A typhoon is an extremely low-pressure system with abundant precipitating waters on the surface and in the air. Typhoons pass through Taiwan and the seas near this island from April to November, and create large gravity variations that are easily detectable at HS and can be used to investigate gravity change caused by atmospheric pressure change, including the effects originating from attraction, loading and inverted barometer [*Boy et al.*, 2003; *Hinderer and Crossley*, 2004; *Riccardi et al.*, 2007]. Finally, the coseismic gravity change at HS due to a nearby earthquake will help to validate the fault parameters associated with the earthquake [*Imanishi et al.*, 2004]. Real-time data of typhoons and earthquakes around Taiwan can be assessed at the Central Weather Bureau of Taiwan (http://www. cwb.gov.tw).

[4] With more than 2 years of SG data available at HS (from March 2006 to present), the objective of this paper is to present results on the quality assessment of the HS SG data and the applications of such data to selected problems. The geological settings and the regional tectonic motion around HS, based on previous geophysical explorations and continuous GPS observations, will also be presented. The calibration factor and the drifting rate of T48 will be estimated from parallel observations of absolute and SG gravity values, and these are two crucial parameters of T48 that must be taken into account when using the SG data at HS. The absolute gravity measurements were collected by

three FG5 gravimeters from Taiwan and France. We will also employ standard models to account for the gravity changes due to atmosphere, groundwater, soil moisture, and polar motion, which help to explain the origins of gravity changes obtained from FG5 and SG observations at HS.

2. Geological Setting and GPS-Derived Regional Tectonic Motion

[5] 5w>As shown in Figure 1, HS lies south of an alluvium created by two major rivers in Hsinchu. There are three nonactive faults near HS. The Hsinchu Fault is within few hundreds of m to HS and is a normal fault lying in the west-east direction with a total length of 9 km. The latest movement of the Hsinchu Fault occurred some 100,000 years ago (Central Geological Survey of Taiwan, http://www.moeacgs.gov.tw), and it is expected that there will be no immediate threat of large ground movement and earthquake at HS due to this fault. HS is at the footwall of the Hsinchu Fault and is situated on the "Toukeshan formation" that has a distinct geological structure from that of the alluvium to the north. The alluvium is fan shaped and contains several soil layers. Figure 2 shows a cross section of the alluvium (Figure 1). The depths of the layer with shallow groundwater range from 10 m to 40 m. Below this surface layer lies several layers composed of gravel and fine sand that can store groundwater. The amount of groundwater in these layers varies with rainfall, which is largely brought by monsoons and typhoons. As such, the seasonal or shorter time scale changes of groundwater over the alluvium will create gravity variations at HS, and will be discussed later in this paper.

[6] Compared to the eastern coast of Taiwan, the western coast of Taiwan is relatively quiet in terms of seismic activity. About 75% of earthquakes in Taiwan happen in the eastern coast, and 25% in the western coast (Central Geological Survey of Taiwan). On the basis of the GPS measuring results and a viscoelastic earthquake cycle model of *Johnson et al.* [2005], the horizontal rates of plate motion in southeastern Taiwan are about $7-8$ cm a^{-1}, while the horizontal rates in the rest of Taiwan are few mm a^{-1} to few cm a^{-1}. In this paper, we used GPS data from four continuous GPS stations (Figure 1), spanning almost the same time period as that of the HS SG data, to study the regional tectonic motion around Hsinchu. Station HCHM is located on the summit of Mt. 18-Peak and is regarded as a colocated station with HS. Station TCMS is in the International GPS Service (IGS) network. Station SHJU is colocated with the Hsinchu tide gauge station. Using the IGS precise GPS orbits (http://igscb.jpl.nasa.gov/) and the Bernese 5.0 software [*Beutler et al.*, 2007], daily coordinates of the four GPS stations were determined and their variations are given in Figure 3. In general, all GPS stations show a consistent southeastward motion at a speed of about $1-2$ cm a^{-1}, and the pattern of horizontal motion in Figure 3 is similar to that given by *Johnson et al.* [2005]. Unlike the vertical motion, a localized and uniform horizontal motion will not create a significant mass change leading to gravity change.

[7] The vertical motions at the four GPS stations range from -3.5 to 0.5 mm a^{-1}. TCMS and NCTU are several hundreds of m from HCHM and are located on the top of a
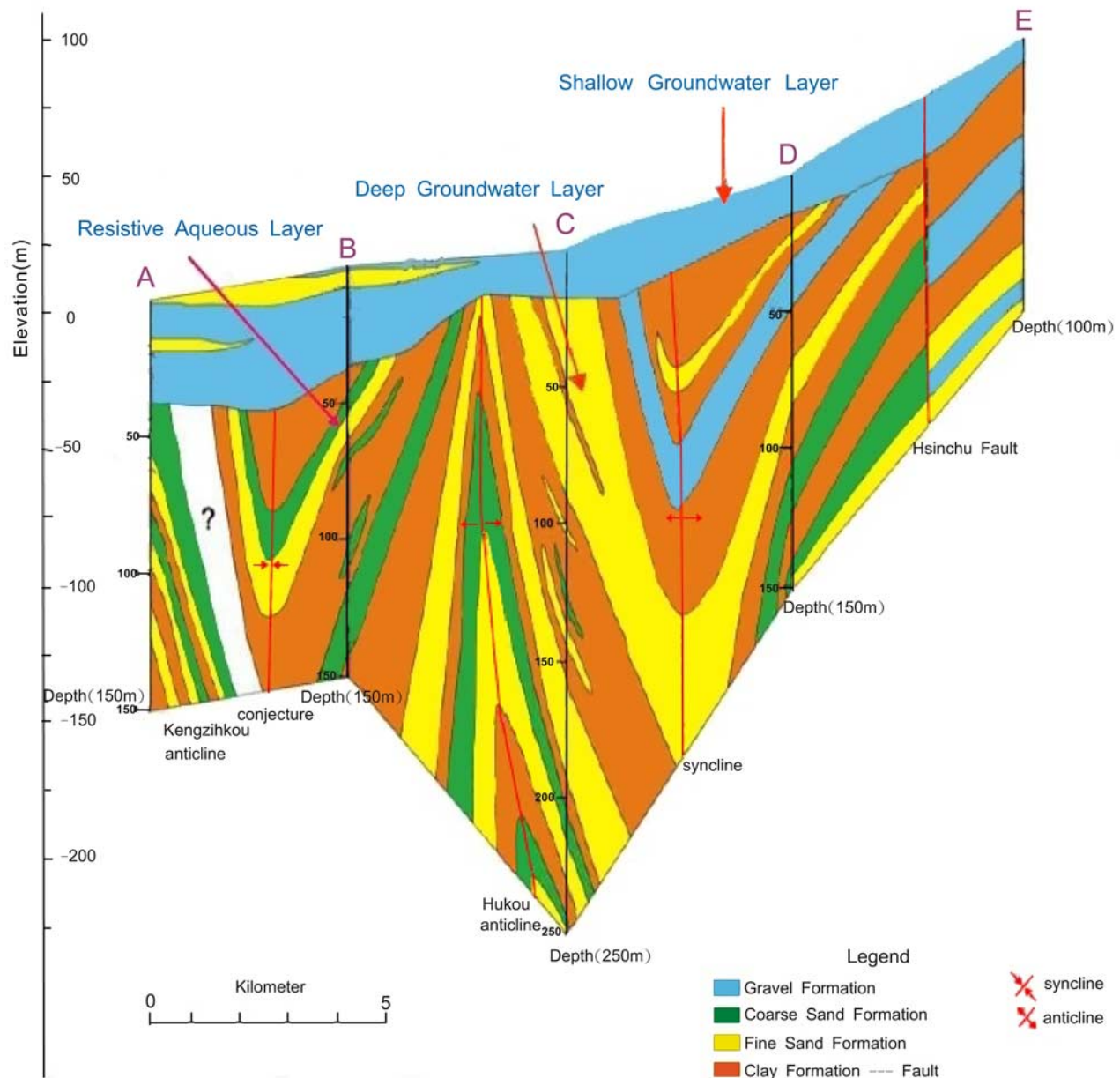
Figure 2. A cross section along the alluvium north of HS showing layers with shallow and deep groundwater. Deep groundwater takes time to fill and will delay groundwater-induced gravity change. The sampling points A, B, C, D, and E are shown in Figure 1.

building. These two stations have been installed for over 10 years. Therefore, the subsidence of the buildings will not contribute to the vertical rates detected by GPS over 2006–2008. The SHJU tide gauge station, installed in 2004, is situated at the Hsinchu fishing harbor. Again the platform housing the SHJU tide gauge should be stable by 2006. The vertical rate of HCHM (also HS) is 0.5 ± 0.3 mm a^{-1}. Since there is neither major man-made structure nor groundwater extraction near HCHM, the vertical motion at HCHM (and therefore at HS) should be of tectonic origin. Furthermore, the vertical rate of HCHM (at the footwall) relative to TCMS (at the hanging wall) is 0.2 ± 0.4 mm a^{-1}, which

shows that the relative vertical displacement between the footwall and the hanging wall of the Hsinchu Fault is small.

3. Parallel Absolute and Superconducting Gravimeter Observations

3.1. Calibration Factor of T48

[8] It is necessary to determine a calibration factor of T48 that converts the raw SG readings to readings in gravity. We determined an optimal calibration factor of T48 using parallel observations of T48 and a FG5 absolute gravimeter (serial 231). The pillars for T48 and FG5 are separated by about 1 m only. This method has been demonstrated by *Francis et al.* [1998], *Imanishi et al.* [2002], and *Tamura et*
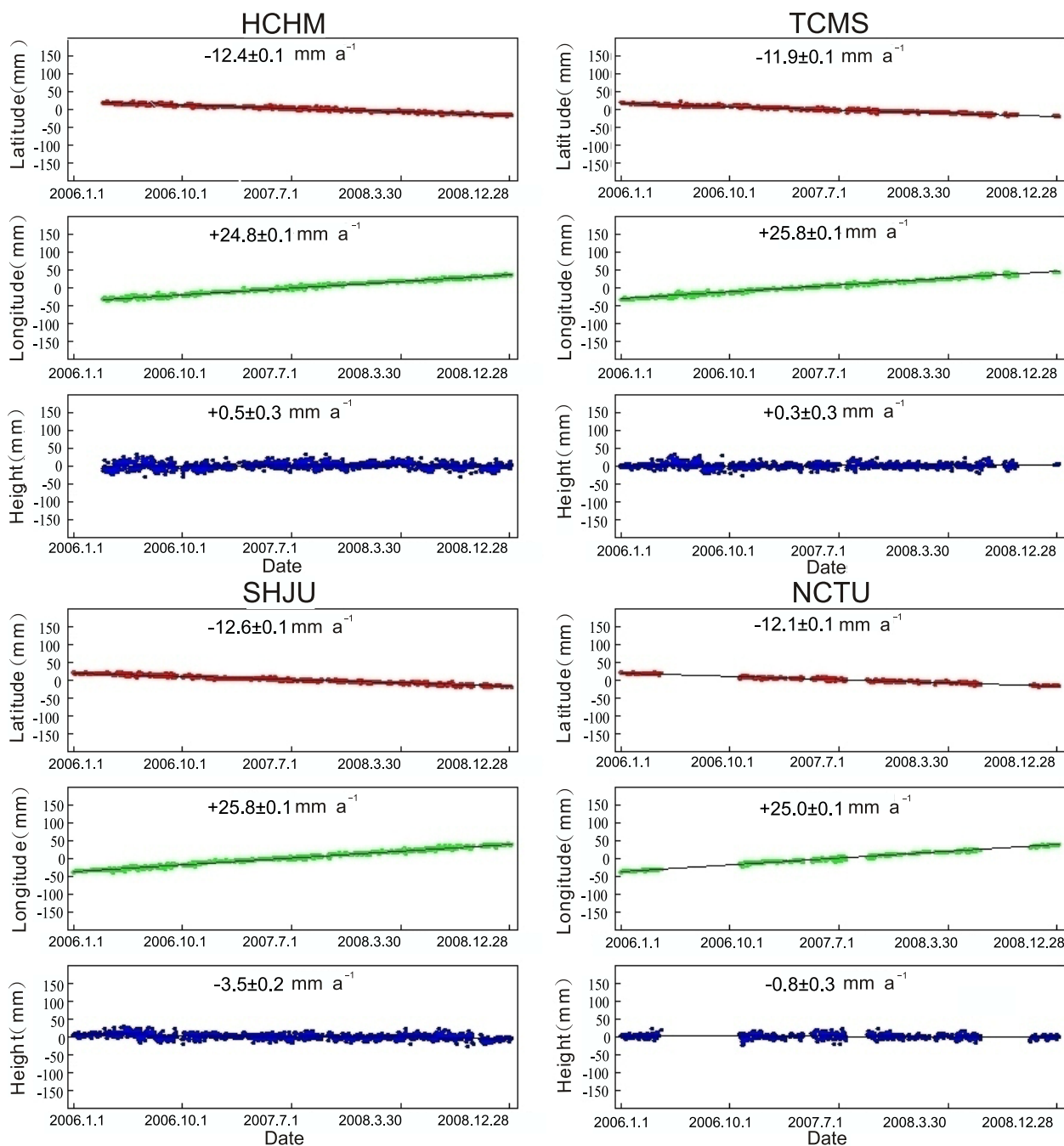
Figure 3. Variations of coordinates at the HCHM, TCMS, SHJU, and NCTU continuous GPS stations. The numbers are linear rates of displacements from least squares fits to the coordinate variations.

al. [2004]. In total, 18 sessions of parallel observations were collected. The following model is adopted for the determination of the calibration factor:

$$g(t) = f_c V(t) + b - st \qquad (1)$$

where f_c is the calibration factor, b is an offset, s is the trend of T48, and g and V are readings from FG5 and T48, respectively. Given the observations (g and V), the standard least squares technique is used to compute f_c, s, and b. FG5 and T48 sense the same gravity effects of solid Earth tide

and ocean tide, as well as any other time-varying gravity effects, to produce gravity variations, which are exactly what we need for determining the calibration factor. Before the least squares solution, the outliers in the T48 and FG5 data, which occur mostly during heavy rainfall, earthquakes, and abrupt changes of air pressure due to typhoons, were removed. As an example, Figure 4 shows the T48 and FG5 data for calibration from the session of 20 June 2006 to 2 July 2006. The variations in the FG5 gravity readings are mainly caused by the body tide and are almost linearly correlated with the SG readings in voltage (correlation coefficient 0.953). The residuals of FG5 observations from
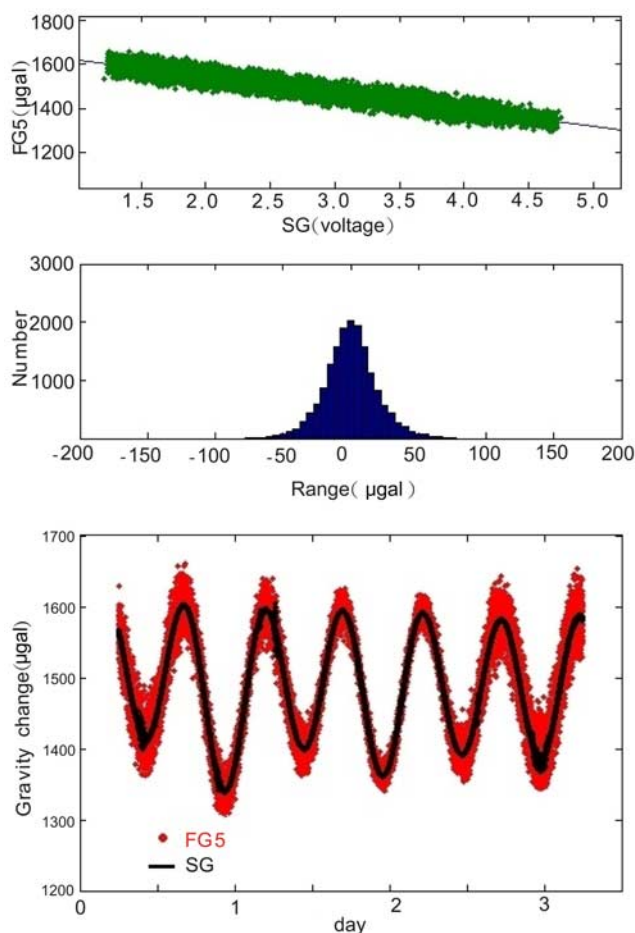
Figure 4. (top) Raw observations of SG and FG5, (middle) histograms of residual FG5 gravity values after the linear regression, (bottom) scaled SG (by the calibration factor) and FG5 observations.

the least squares adjustment (raw FG5 gravity values minus fitted gravity values) follow the normal distribution, suggesting that the linear model in equation (1) is adequate, and the estimated parameters are unbiased.

[9] Table 1 lists the 18 parallel sessions and some useful information about the FG5 observations. Using all data from the 18 sessions, we obtained a calibration factor of -75.96 ± 0.07 μGal V^{-1} for T48. The trend s of T48 is $1.41 \pm 0.09 \mu$Gal a^{-1}. Note that this calibration factor (-75.96 μGal V^{-1}) was determined using all FG5 and T48 observations simultaneously in one least squares solution, rather than the average of the individual calibration factors from the 18 sessions in Table 1. A calibration factor based on just one session in Table 1 is considered less reliable. The standard error (0.07 μGal V^{-1}) is smaller than 0.1 μGal V^{-1}, which is in general an acceptable value in the SG community [*Tamura et al.*, 2004]. The uncertainty in the calibration factor is largely caused by the random errors in the FG5 observations. As mentioned before, HS is only 8.6 km from the sea, so the set scatters of FG5 observations (from 1.3 to 4.1 μGal; Table 1) are larger than what would be expected at a "quiet" station, where a typical set scatter is below 1 μGal. The calibration factor of T48, to be

published on the GGP web site, will be constantly improved as more parallel FG5 and T48 observations are available in the future. Since the calibration factor of T48 obtained in this paper has already been very precise, we expect only a minor change in future updated values.

3.2. Drift of T48

[10] The drift of a superconducting gravimeter will lead to a false interpretation of the long-term gravity change at the SG site. Figure 5 shows the parallel FG5 and SG observations from 2006 to 2008, with the solid tide and ocean tide gravity effects and anomalous values removed. Some of the gravity values were collected by FG5 No. 224 (from Taiwan) and 228 (from France) when FG5 No. 231 (from Taiwan) was on the fieldwork. These two time series of gravity, sampled at different time intervals, show a dominant annual cycle and an increasing trend. A gravity measurement from FG5 or T48, $g(t)$, can be modeled as

$$g(t) = g_0 + \dot{g}t + c \cos wt + d \sin wt + e(t) \qquad (2)$$

where t is time, g_0 is a constant, $\dot{g}$ is the linear change rate, c and d are the coefficients of the annual cycle, w is the annual frequency, and e is the measurement noise. Least squares estimations were then employed to determine the four parameters in equation (2). The amplitude and phase were determined as $\sqrt{c^2 + d^2}$ and $\tan^{-1}(d/c)$. As a result, the amplitudes of the annual cycle from FG5 and T48 are 5.9 and 6.3 μGal, and the phases are $-22.9°$ and $-26.1°$. The difference in phase is partly due to data errors and partly due to the two different ways of sampling FG5 and SG measurements. The measurements of SG were almost continuous (sampling rate is 1 HZ) from March 2006 to present, but the measurements of FG5 were taken at the times given in Figure 5, and each FG5 gravity value was the average over several drops. The linear change rates from FG5 and T48 are 2.2 ± 0.7 and 2.4 ± 0.2 μGal a^{-1}. If we assume that the rate obtained by the FG5 gravimeters is a true rate of gravity change, the instrumental drift of T48 is

Table 1. Sessions of Parallel Superconducting and Absolute Gravity Observations for Determining the Calibration Factor of T48

| Starting Time of Session (GMT)	Length (h)	FG5 Set Scatter (μGal)	Total Uncertainty (μGal)	Number of Drops
6h, 5 June 2006	30	4.1	2.1	3479
1h, 9 June 2006	29	2.5	2.1	3500
6h, 13 June 2006	24	2.3	2.1	2807
2h, 21 June 2006	48	1.5	2.0	5716
3h, 30 June 2006	48	1.3	2.0	5746
5h, 7 July 2006	95	2.3	2.1	10772
9h, 11 October 2006	19	3.4	2.2	2224
6h, 4 November 2006	24	2.7	2.1	4109
3h, 17 November 2006	24	2.4	2.4	4713
8h, 2 March 2007	39	2.2	2.1	4668
7h, 4 March 2007	72	3.7	2.1	8427
12h, 10 November 2007	28	3.3	2.2	6123
9h, 30 November 2007	72	2.2	2.0	17242
0h, 16 December 2007	72	1.7	2.0	17018
0h, 2 January 2008	24	2.5	2.1	5399
0h, 7 January 2008	72	2.0	2.1	16789
0h, 6 February 2008	48	3.1	2.1	11510
0h, 21 February 2008	72	1.8	2.1	16713
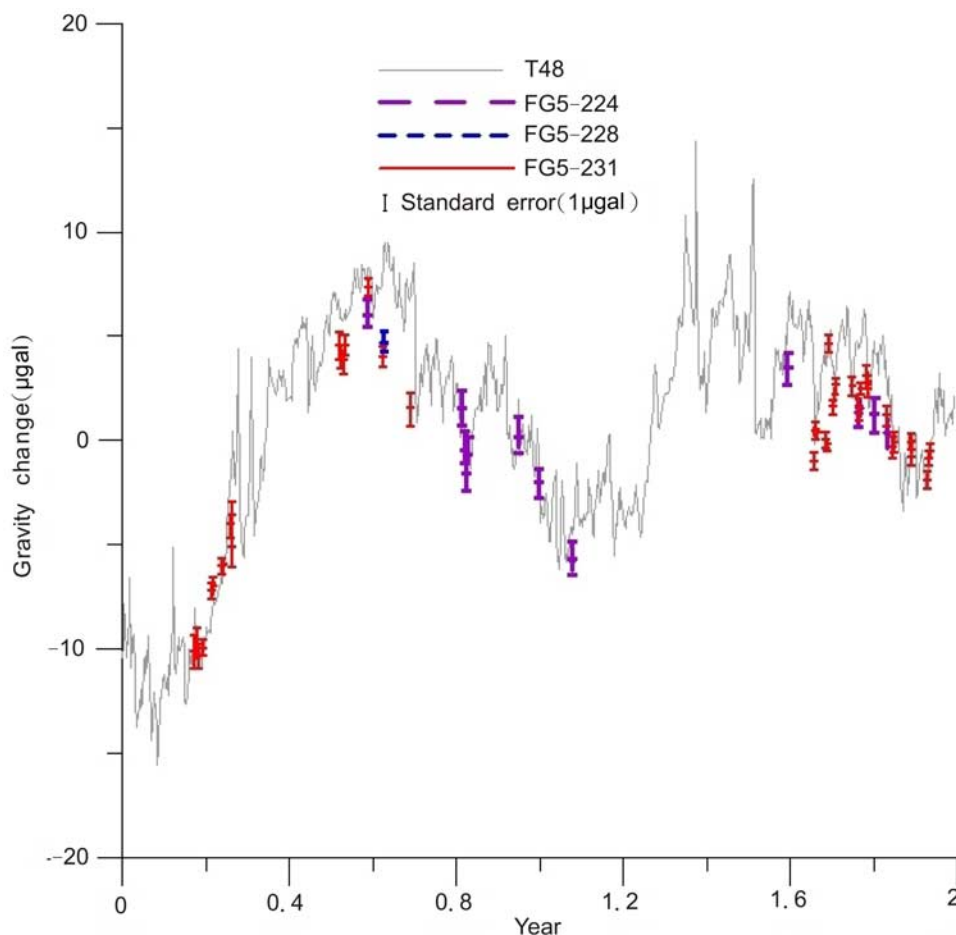
Figure 5. Comparison of SG and FG5 measurements to determine the drift of T48. The FG5 gravimeter number 228 is from France, while numbers 224 and 231 are from Taiwan.

estimated to be at a rate of 0.2 ± 0.7 μGal a^{-1}. Note that this drifting rate (0.2 μGal a^{-1}) is estimated using the absolute gravity observations (serials 224, 228, and 231) from three FG5 absolute gravimeters. It differs from the trend (1.4 μGal a^{-1}) estimated in section 3.1. This is explained by the fact that the trend in equation (1) may also absorb other unmodeled effects in the determination of the calibration factor and may not truly reflect the drift of T48.

4. Tidal Analysis and Observed Tide

4.1. Preprocessing of the Observed SG Data

[11] Before the tidal analysis, using the software "TSOFT" provided by the International Center for Earth Tides (ICET, http://www.astro.oma.be/ICET/), the SG data of T48 were despiked, filtered and decimated to hourly records for spectral analysis. Figure 6 shows the spectrum of the raw SG gravity records. As expected, we observe the six leading tidal components of M_2, K_1, S_2, O_1, N_2 and P_1 (in decreasing order of amplitude). Note the distinct signal component labeled M_3 in Figure 6 at a frequency of about 2.9 cycle d^{-1}, which is due to the M_3 ocean tide modulated by the complex bathymetry and coastal lines around the Taiwan Strait. This shows that, as pointed out by *Hinderer and Crossley* [2004] and *Boy et al.* [2004], SG provides

interesting and important data to study nonlinear tides over such a shallow water area as the Taiwan Strait.

4.2. Tidal Analysis

[12] We compared the two computer programs ETERNA [*Wenzel*, 1996] and BAYTAP-G [*Tamura et al.*, 1991] for tidal analysis. Tables 2 and 3 summarize the amplitude factors and phases along with the standard (formal) errors for the short-period tides obtained by ETERNA and BAYTAP-G, respectively. A phase shown in Table 2 and 3 is given as the phase difference from the equilibrium body tide whose amplitude changes with the astronomical argument of each tidal constituent. The standard errors in Tables 2 and 3 suggest that the estimated amplitudes and phases are statistically meaningful. The tidal parameters obtained from the two computer programs are quite consistent. As expected, the standard errors increase with the tidal periods. The M_2 wave, the most dominant component in the gravity time series, has the least standard error in both amplitude factor and phase. The phase of ψ_1 constituent shows a large formal error exceeding $1°$, which may be reduced when a longer SG record than 2 years is available for the analysis.

[13] To reduce the analysis error due to the contamination of the effect caused by atmospheric pressure changes, the
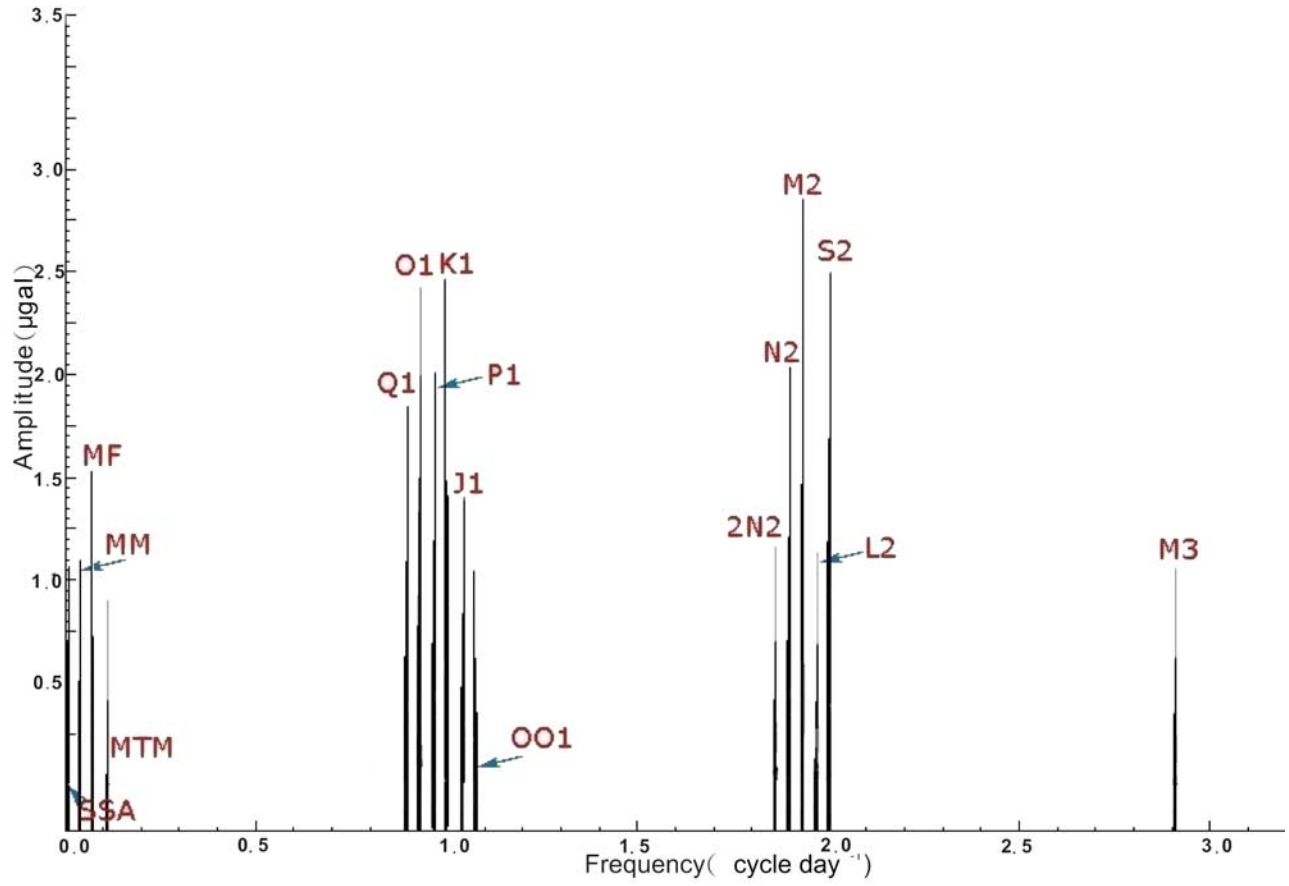
Figure 6. Tidal spectrum (in logarithm scale) from 2 years of raw gravity records of T48. Two clusters are present at the semidiurnal and diurnal wave bands. Tides with periods shorter than the M_3 period are not shown here.

pressure term was included in the tidal analysis as a term to be estimated. By using the barometer data simultaneously obtained at HS with the SG data, we obtained the gravity-atmospheric admittances of -0.340 ± 0.003 and -0.355 ± 0.003 μGal hPa^{-1} from ETERNA and BAYTAP-G, respectively. Although the two computer programs ETERNA and

BAYTAP-G are developed independently, they produce gravity-atmosphere admittances consistent to 97%. These values represent a mean value for the gravity-atmosphere of the HS SG that is averaged over the 2 years. As we will discuss in section 5, the gravity-atmosphere admittance will vary with the spatial and temporal scales of the atmospheric pressure change.

Table 2. Tidal Analysis Results by ETERNA

Wave	Amplitude (μGal)	Amplitude Factor	Phase (°)
Q_1	5.649 ± 0.008	1.2485 ± 0.0018	-1.34 ± 0.08
O_1	29.061 ± 0.008	1.2298 ± 0.0003	-2.28 ± 0.02
M_1	2.251 ± 0.007	1.2119 ± 0.0036	-2.50 ± 0.17
P_1	13.125 ± 0.010	1.1939 ± 0.0009	-2.74 ± 0.04
S_1	0.317 ± 0.014	1.2178 ± 0.0541	2.54 ± 2.55
K_1	39.145 ± 0.009	1.1784 ± 0.0003	-2.84 ± 0.01
ψ_1	0.331 ± 0.009	1.2712 ± 0.0355	-5.38 ± 1.60
ϕ_1	0.584 ± 0.010	1.2348 ± 0.0209	-0.96 ± 0.97
J_1	2.191 ± 0.008	1.1791 ± 0.0045	-3.36 ± 0.22
OO_1	1.173 ± 0.005	1.1544 ± 0.0049	-2.51 ± 0.24
$2N_2$	2.314 ± 0.011	1.2232 ± 0.0058	1.86 ± 0.27
N_2	13.947 ± 0.014	1.1773 ± 0.0012	-3.40 ± 0.06
M_2	71.452 ± 0.014	1.1548 ± 0.0002	-3.03 ± 0.01
L_2	1.817 ± 0.018	1.0388 ± 0.0104	-0.81 ± 0.58
S_2	33.093 ± 0.014	1.1497 ± 0.0005	-1.63 ± 0.02
K_2	9.033 ± 0.011	1.1550 ± 0.0014	-1.59 ± 0.07
M_3	1.203 ± 0.003	1.0908 ± 0.0024	-0.31 ± 0.12

Table 3. Tidal Analysis Results by BAYTAP-G

| Wave	Tidal Amplitude (μGal)	Amplitude Factor	Phase (°)
Q_1	5.646 ± 0.017	1.2482 ± 0.0037	-1.45 ± 0.17
O_1	29.056 ± 0.016	1.2299 ± 0.0007	-2.28 ± 0.03
M_1	2.239 ± 0.011	1.2053 ± 0.0060	-2.51 ± 0.29
P_1	13.117 ± 0.016	1.1933 ± 0.0015	-2.65 ± 0.07
S_1	0.309 ± 0.004	1.1874 ± 0.0142	-2.12 ± 0.69
K_1	39.149 ± 0.014	1.1783 ± 0.0004	-2.83 ± 0.02
ψ_1	0.309 ± 0.004	1.1888 ± 0.0157	-2.96 ± 0.76
ϕ_1	0.563 ± 0.007	1.1896 ± 0.0153	-2.85 ± 0.74
J_1	2.193 ± 0.012	1.1801 ± 0.0066	-3.34 ± 0.32
OO_1	1.176 ± 0.007	1.1573 ± 0.0068	-2.86 ± 0.34
$2N_2$	1.919 ± 0.003	1.2247 ± 0.0020	1.81 ± 0.09
N_2	13.947 ± 0.005	1.1778 ± 0.0004	-3.36 ± 0.02
M_2	71.435 ± 0.005	1.1550 ± 0.0001	-3.03 ± 0.00
L_2	1.831 ± 0.006	1.0473 ± 0.0033	-0.75 ± 0.18
S_2	33.057 ± 0.004	1.1488 ± 0.0001	-1.89 ± 0.01
K_2	9.031 ± 0.003	1.1546 ± 0.0004	-1.63 ± 0.02
M_3	1.206 ± 0.002	1.0942 ± 0.0018	-0.16 ± 0.10
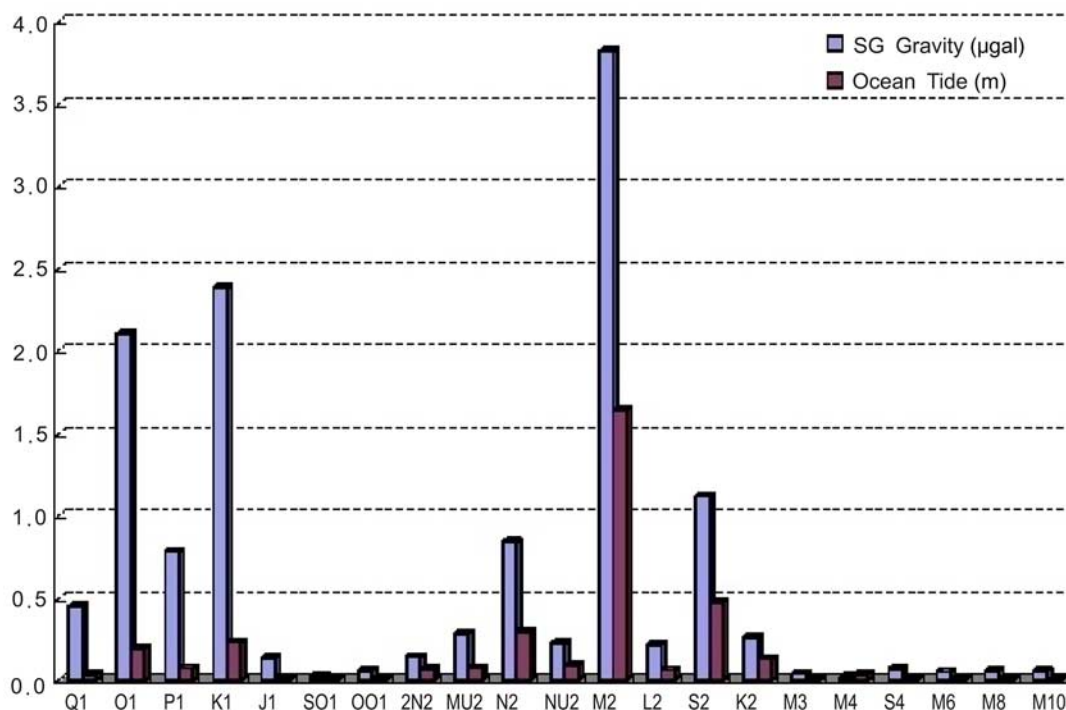
Figure 7. Amplitudes of ocean tide from tide gauge records at the Hsinchu Harbor (9 km to HS), and amplitudes of OTGE from the SG gravity measurements at HS (amplitudes of OTGE are the same as the ones given in the column "T48" in Table 4).

4.3. Ocean Tide Gravity Effect

[14] We model the ocean tide gravity effect (OTGE) according to the Green's function approach, which is represented by

$$\Delta g = \frac{G\rho_w}{R^2} \int \int \frac{h(\phi,\lambda)(p-u)}{(1+p^2-2pu)^{3/2}} ds - \rho_w \int \int h(\phi,\lambda)K(\psi)ds \tag{3}$$

where G is the Newtonian gravitational constant, ρ is the density of seawater, R is the mean Earth radius, h is tidal height (depending on latitude ϕ and longitude λ), ψ is spherical distance, $u = \cos\psi$, $p = (R+H)/R$, $ds = R^2 \cos\phi d\phi d\lambda$, and K is Greens' function based on the loading love numbers of *Farrell* [1972]. The first and second terms of the right-hand side of equation (3) represent the effects of attraction and loading, respectively. The detail of our OTGE model and software development is given by *Huang et al.* [2008]. Note that the Newtonian (attraction) effect depends on station height H through variable p.

[15] In the Taiwan Strait, the amplitude of the M_2 ocean tide increases toward the central part of the Strait and it reaches a maximum (about 2.2 m) at a latitude about 24°N, and then decreases almost linearly northward to the East China Sea and southward to the South China Sea. Also, there is a standing M_2 ocean tide near the central Taiwan Strait [*Jan et al.*, 2004]. As an example, the M_2 amplitudes at Keelung (25.2°N, near the East China Sea), Hsinchu (24.8°N, near HS) and Pintung (22.0°N, near the South China Sea) are 0.6, 1.6 and 0.2 m, respectively.

[16] SG observations can also be used to estimate OTGE, as carried out by *Boy et al.* [2003]. This is achieved by removing an adopted body tide model from the SG data, along with all the other known, well-modeled signals, so that the residual SG gravity values are assumed to contain the OTGE signal only. However, such an estimated OTGE will be highly dependent on the adopted body tide model. As an experiment, we removed the body tide of *Dehant et al.* [1999] (hereafter referred to as DDW) from the raw SG gravity records. The remaining gravity values were then used to estimate OTGE at HS by ETERNA software. The estimated OTGE will be then called the "observed" OTGE. Figure 7 shows the amplitudes of the "observed" OTGE at HS and the amplitudes of the ocean tide at the SHJU tide gauge station (Figure 1). In the amplitude spectra of Figure 7, six leading components are identified: O_1, P_1, K_1, N_2, M_2 and S_2. It is interesting to note that the relative magnitudes of these constituents are different between the OTGE and the ocean tide. For OTGE, the order is M_2, O_1, K_1, S_2, N_2, and P_1, while for the ocean tide, the order is M_2, S_2, N_2, K_1, O_1, and P_1. For both the ocean tide and its gravity effect, the M_2 component is dominant. For ocean tide, M_2 contributes 47% to the total signal, while for OTGE the M_2 contribution is only 23%. In addition to M_3, several other nonlinear tides are also present in Figure 7. The SG observations at HS can be used to study nonlinear tides in the Taiwan Strait, as was done by *Boy et al.* [2004] for European shallow waters.

[17] Table 4 compares the amplitudes and phases of OTGE from the observations (T48) and from the NAO.99b [*Matsumoto et al.*, 2000], FES2004 [*Lyard et al.*, 2006] and CSR4.0 [*Eanes and Bettadpur*, 1996] ocean tide models for eight short-period waves. Overall, the OTGE from the

Table 4. Amplitudes and Phases of Ocean Tide Gravity Effect at Hsinchu From T48 Observations and From NAO.99b, FES2004, and CSR4.0 Ocean Tide Models

Wave	T48	NAO.99b	FES2004	CSR4.0
M_2	3.82[a]	3.76	3.37	2.85
	−98.0[b]	−99.6	−91.8	−122.2
N_2	0.84	0.82	0.75	0.93
	−79.1	−76.7	−58.9	−56.5
S_2	1.12	0.95	0.87	0.82
	−110.5	−114.4	−86.4	−42.7
K_2	0.26	0.24	0.25	0.31
	−103.1	−108.0	−81.9	−30.4
K_1	2.38	2.40	2.15	2.47
	−54.2	−55.1	−51.1	−58.9
O_1	2.10	2.08	2.01	2.13
	−33.2	−30.8	−34.1	−30.6
P_1	0.78	0.78	0.71	0.82
	−53.0	−52.8	−53.1	−56.7
Q_1	0.45	0.44	0.41	0.48
	−17.4	−22.4	−23.8	−23.3

[a]Amplitude in μGal.
[b]Phase in degrees.

NAO.99b tide model agrees the best with the SG observations in both amplitudes and phases of all tidal components. The model assessment by *Penna et al.* [2007] at TWTF, a continuous GPS station in Taiwan some 30 km north of HS, also shows that, compared to FES2004, the ground displacements predicted with NAO.99b are more consistent with the GPS observed displacements. The discrepancies in amplitude are at the submicoGal order, except for the M_2 from CSR4.0. Compared with the diurnal tides, the modeled phases of the semidiurnal tides show relatively large discrepancy, showing the complexity in the variations of the semidiurnal tides in the Taiwan Strait. Therefore, there is room for improvement of the tide models listed in Table 4, especially in the phases of the semidiurnal tides.

[18] Since HS is near the Taiwan Strait, the Newtonian gravity effect of the ocean tide can be significant. Using the NAO.99b tide model, we find that at HS the loading effect and the Newtonian effect of M_2 are 3.01 and 0.75 μGal, respectively. Thus the Newtonian effect contributes 20% to the total effect. As shown in equation (3) and demonstrated by *Lysaker et al.* [2008], the Newtonian gravity effect is height-dependent. As an example, Table 5 shows such a height dependence at HS and Lulin for M_2. Station Lulin (latitude = 24.47109°N and longitude = 120.88081°E) will house the second SG (T49) of Taiwan, and is about 74.5 km to the Taiwan Strait and 60.7 km to the Pacific. At both HS and Lulin, the Newtonian effect increases with elevation, and this is due to an increasing vertical component of the attraction as the elevation becomes larger. Lulin is distant from the sea in comparison to HS (74.5 versus 8.6 km to the Taiwan Strait), so the Newtonian effect at Lulin is less sensitive to elevation change than that at HS.

[19] At a given SG station near the sea, the spatial variation of tidal height can be assumed to be linear. With this assumption and following the method for evaluating the innermost zone contribution of gravity anomaly to geoid [*Heiskanen and Moritz*, 1985], one finds the near-zone Newtonian effect of ocean tide as

$$g_i = C \frac{G s_0 \rho h}{4 \pi R} \quad (4)$$

where s_0 is the radius of the near-zone zone, C is the ocean/land ratio near the station, and s_0 is the maximum distance that a linear variation of tidal height around the station holds. On the basis of the amplitude variation of M_2 in the Taiwan Strait [*Jan et al.*, 2004], s_0 is about 10 km. Thus, for a station near the sea, the Newtonian effect is proportional to the tidal height. Using the integrations in equation (3) and the NAO.99b tide model, the largest Newtonian effect of ocean tide is found to be near Matzu, which is an island in northwestern Taiwan Strait and offshore mainland China. For example, at a permanent GPS tracking station on this island that is 500 m from the sea, the amplitudes of the M_2 tide for the loading and Newtonian effects are 6.07 and 5.33 μGal, respectively. This implies that for a gravity station on an island, the Newtonian gravity effect of ocean tide is about the same as the loading effect.

4.4. Comparison With Theoretical Body Tide

[20] In order to demonstrate the uniqueness of the HS SG station at its latitude (about 25°N) and the effect of OTGE correction, we compare the observed (this study) and the theoretical amplitude factors for selected waves in Table 6. The theoretical amplitude factors in Table 6 are given by the DDW model for the elastic and inelastic Earth, which are derived using the PREM Earth model [*Dziewonski and Anderson*, 1981]. The DDW amplitude factors are latitude-dependent and can be expressed by

$$\delta_i^d = a_i^d + b_i^d \frac{\sqrt{6}}{4} (7 \sin^2 \phi - 3)$$
$$\delta_i^s = a_i^s + b_i^s \frac{\sqrt{3}}{2} (7 \sin^2 \phi - 1) \quad (5)$$

where ϕ is latitude, subscript i stands for tidal component, and superscripts d and s stand for diurnal and semidiurnal waves, respectively. The second terms in equation (5) are the latitude-dependent terms contributing ∼0.4% to the amplitude factors; see also *Torge* [1989, pp. 398]. A "relative difference" in Table 6 is defined as the ratio between the absolute difference (observation − model) and the observation. Three global ocean tide models, NAO.99b, FES2004, and CSR4.0, were used to correct for the OTGE in the SG data.

[21] The amplitude factors corrected for OTGE agree better with the model factors of DDW than the factors from the raw SG data. We observed in Table 6 that, in general, the inelastic model of DDW agrees better with the observations of T48 than the elastic model. Among three ocean models compared here, NAO.99b gives the corrected amplitude

Table 5. Amplitude of the Newtonian Effect of M_2 Ocean Tide as a Function of Height at the Superconducting Gravimeter Stations of Hsinchu and Lulin

Height (m)	HS (μGal)	Lulin (μGal)
0	0.66	0.69
100	0.70	0.69
200	0.80	0.69
300	0.93	0.70
400	1.08	0.70
500	1.25	0.70

Table 6. Amplitude Factors From T48 Observations and the DDW Model[a]

Wave	Factor From Theory		T48 Corrected by NAO.99			T48 Corrected by FES2004			T48 Corrected by CSR4.0		
	Elastic	Inelastic	Factor	Elastic[b]	Inelastic[b]	Factor	Elastic[b]	Inelastic[b]	Factor	Elastic[b]	Inelastic[b]
ψ_1	1.2344	1.2656	1.3153	6.15	3.78	1.3088	5.68	3.30	1.3200	6.48	4.12
$\varnothing_1$	1.1672	1.1696	1.2175	4.13	3.93	1.2177	4.15	3.95	1.2186	4.22	4.02
OO_1	1.1547	1.1561	1.1556	0.08	0.043	1.1555	0.07	−0.05	1.1557	0.09	−0.03
K_1	1.1335	1.1355	1.1416	0.71	0.53	1.1420	0.74	0.57	1.1444	0.95	0.78
O_1	1.1527	1.1542	1.1661	1.15	1.02	1.1701	1.48	1.36	1.1646	1.02	0.89
N_2	1.1603	1.1617	1.1724	1.03	0.91	1.1500	−0.90	−1.02	1.1531	0.62	−0.75
P_1	1.1479	1.1493	1.1501	0.19	0.07	1.1541	0.54	0.42	1.1521	0.36	0.24
K_2	1.1603	1.1617	1.1640	0.32	0.20	1.1532	−0.62	−0.74	1.1304	2.65	2.77
Q_1	1.1527	1.1542	1.1379	−1.30	−1.43	1.1459	−0.59	−0.72	1.1308	−1.94	−2.07
M_2	1.1603	1.1617	1.1645	0.36	0.24	1.1564	−0.34	−0.46	1.1802	1.69	1.57
S_2	1.1603	1.1617	1.1623	0.17	0.05	1.1470	−1.16	−1.28	1.1278	2.88	3.01
M_3	1.0724	1.0734	1.0927	1.86	1.77	1.0926	1.85	1.76	1.0926	1.85	1.76

[a]DDW, *Dehant et al.* [1999].
[b]Relative difference in %.

factors which are most consistent with the factors expected from the theory. In this case, if we take the mean value for the six major tidal constituents having an amplitude exceeding 10 μGal (i.e., K1, O1, P1, N2, M2, and S2), the relative difference for the inelastic model is smaller by about 22% than that for the elastic model, i.e., ratio of $(0.602 - 0.470)/0.602$. Moreover, for the mean of the same 6 constituents, we point out that the inelastic amplitude factor from the DDW (i.e., 1.1540) is systematically smaller by about 0.5% than the observed one (i.e., 1.1595) corrected by NAO.99b. Compared with the calibration error of 0.07% described in section 3, the difference of 0.5% is significant in the discussion of the tidal factor. It is necessary to further improve the accuracy of the ocean tide correction to make concrete conclusions on this, especially for the M_2 and O_1 constituents, which have large amplitude and are far from the effect of the free core resonance [e.g., *Wahr*, 1981] appearing around the frequency of K_1 and ψ_1 constituents.

5. Atmospheric Pressure Effect

[22] Using 2 years of SG and barometric data at HS, we obtained average gravity-atmosphere admittances of -0.340 ± 0.003 and -0.355 ± 0.003 μGal hPa^{-1} from ETERNA and BAYTAP-G, respectively. Note that the gravity-atmosphere admittance is frequency-dependent [*Riccardi et al.*, 2007], but this subject is not pursued here. In the following, we will interpret gravity-atmosphere admittances for various atmospheric conditions, including typhoons. As shown by *Ooe and Hanada* [1982], the distribution of air mass can be approximated by an exponential function, in which the density change $\Delta\rho$ at a spot with a spherical angle θ_i to a given station is represented by

$$\Delta\rho = \Delta\rho_0 e^{-|\theta_i|/\alpha} \qquad (6)$$

where α is the horizontal scale (in the same units as the spherical angle) of the atmospheric pressure change. In this paper, we adopt $\Delta\rho_0 = 1.225$ kg m^{-3} for HS. In a normal case of slow and smooth pressure changes, the synoptic horizontal scale is about 1000 km or more, and the temporal scale is about 3 days to 7 days. With the approximation in equation (6), the analytical solution of the Newtonian

attraction of the air mass, expressed as admittance in μGal hPa^{-1}, can be written as [*Ooe and Hanada*, 1982]

$$\Delta g_A = -0.43$$
$$\cdot \left[1 - \sum_{i=1}^{n} \left(\sqrt{\frac{1 - \cos\theta_i}{2}} - \sqrt{\frac{1 - \cos\theta_{i-1}}{2}} \right) e^{-0.5|\theta_{i-1} + \theta_i|/\alpha} \right]$$
$$(7)$$

where n is the total number of segments of the coaxial rings centered at an observation site. Also, the loading (elastic) effect of atmosphere can be estimated by numerically convolving air mass and the loading Green's function as in the case of the ocean tide loading effect (see equation (3)). The oceans respond to atmospheric pressure changes as an inverted barometer (IB) over wide frequency bands [*Wunsch and Stammer*, 1997], and the observations indicate that this hypothesis is well realized in the frequency band lower than about 0.1 cycle d^{-1} [*Matsumoto et al.*, 2006]. If the IB response is completely established, there will be no loading effect due to atmospheric pressure changes over the oceans, while in the case of the non-IB response (NIB), the same loading effect is expected on sea and land. To compare the computations on the basis of conditions of the IB and NIB, we used two topographic maps of ETOPO2 on a $2' \times 2'$ grid for the oceanic area around Taiwan, i.e., over a region covering 20°N–30°N in latitude and 116°E–120°E in longitude (ETOPO2 is available from http://www.ngdc.noaa.gov/mgg/fliers/01mgg04.html). A $0.5° \times 0.5°$ land-masking map as used in NAO.99b was employed. A computer code modified from "GOTIC" [*Sato and Hanada*, 1984] was used.

[23] Figure 8 shows the gravity-atmosphere admittances at HS for the cases of IB and NIB. The dependency of the Newtonian and loading effects upon the horizontal scale (α) is given in Figure 8. Figure 8 suggests that the difference in the admittances between the cases of IB and NIB becomes evident at 1°. This is due to the fact that the loading effect decreases rapidly as the horizontal scale decreases. The IB hypothesis is well established at the horizontal scales of 10°–12°. The admittances due to the Newtonian atmospheric effects in the cases of IB and NIB are nearly identical at all horizontal scales. As shown in Figure 8, the
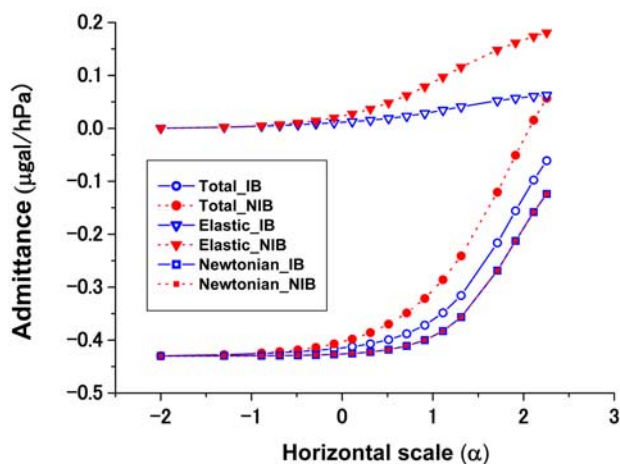
Figure 8. Gravity-atmosphere admittances at HS as a function of horizontal scale (in degree and in logarithm scale) in the cases of IB and NIB oceanic response to atmospheric pressure change. The admittances of the Newtonian effect for IB (blue square) almost coincide with those for NIB (red square).

average observed admittance of -0.350 Gal hPa^{-1} at HS corresponds to the admittance associated with $\approx 10°$ in the case of IB response. Although a rigorous treatment of the Newtonian atmospheric effect should be based on a three-dimensional density model of atmosphere [*Neumeyer et al.*, 2004; *Llubes et al.*, 2004], especially for the seasonal variations in the atmospheric pressure effect on SG observations, the present computation indicates that the mean observed admittance over 2 years mainly reflects the effect of pressure variations at the synoptic scale.

[24] It turns out that the observed admittances during typhoons are far from the mean admittance. A typhoon is a very low-pressure system that might create a large gravity change. In the western Pacific, a typhoon might occur anytime from April to November. Table 7 lists the gravity-atmosphere admittances for the typhoons over 2006–2007 that caused anomalous gravity changes at HS. Some of the parameters of the typhoons are also given in Table 7. The mean of these 8 admittances is -0.45 Gal hPa^{-1}, which is 30% larger than (in magnitude) the mean value of -0.35 Gal hPa^{-1} at Hs. This phenomenon can be explained in part by the horizontal scale of a typhoon (Figure 8), and the temporal scale of the variation of a typhoon. In general, the horizontal scale of a typhoon is only few degrees, which corresponds to a distance range where the contribution of loading effect is very small. Moreover, the speed of typhoon

is typically 30 km hour^{-1} to 40 km hour^{-1}, which is far from the frequency range where the IB hypothesis is well established. The combined effect of the small horizontal scale and the fast motion of air will shift the admittance from -0.35 Gal hPa^{-1} to a value of about -0.43 Gal hPa^{-1}, which is the lowest value obtained from the model computation here.

[25] In addition to the spatial and temporal scales that result in different admittances for the typhoon and non-typhoon conditions, other factors may also affect the admittance during a typhoon, for example, the actual density of the central part of a typhoon. A typical Doppler radar image of typhoon (see, e.g., the real-time radar images at Central Weather Bureau of Taiwan) shows that the precipitating water is not evenly distributed within the effective area of a typhoon and the convection within a typhoon can be asymmetric [see, e.g., *Chou et al.*, 2008; *Li et al.*, 2008]. In particular, condensation of water vapor contained in the moist air normally occurs at low altitudes. Flooding and increased soil moisture will also lead to additional gravity changes. Therefore, the gravity changes due to typhoons detected at HS can be used to validate models of density distribution within a typhoon system, e.g., the model of *Chou et al.* [2008] that is based on three-dimensional variational data assimilation (3DVAR) and the Advanced Microwave Sounding Unit (AMSU) data.

6. Coseismic Gravity Change due to Earthquake

[26] HS is close to an active earthquake zone belonging to the ring of fire in the western Pacific. Near real-time records of earthquakes around Taiwan can be found at http://www.cwb.gov.tw/V5/seismic/quake.htm. An earthquake will introduce oscillations in the gravity records. Depending on the magnitude, depth and distance to HS, the oscillation may last from few minutes to few hours. Such oscillations are considered as anomalous records and are often excluded from such analyses as body tide and ocean tide gravity effects. Hidden in the oscillations is a permanent gravity change that is caused by mass change and surface disloca-tion. The detection of such a permanent gravity change will require the modeling of a step function before and after the earthquake [*Imanishi et al.*, 2004]. Following the method used by *Imanishi et al.* [2004], we used the T48 records to determine permanent gravity changes due to earthquakes around Taiwan in 2006 and 2007, which are listed in Table 8. As an example, Figure 9 shows the permanent gravity change at HS due to an earthquake on 6 September 2007. The magnitude of this earthquake is 6.6 and the depth is 54 km. Situated at the Pacific Ocean northeast of Taiwan, the earthquake's epicenter is at latitude $= 24.28°$ and

Table 7. Gravity Changes due to Typhoons and Gravity-Atmosphere Admittances at Hsinchu

| Typhoon	Date	Center Pressure (hPa)	Category	Pressure Change (hPa)	Gravity Change (μGal)	Admittance (μGal hPa^{-1})
Chanchu	16 May 2006	960	2	11	5.5	-0.47
Bilis	12 July 2006	985	1	28	8.6	-0.45
Kaemi	23 July 2006	960	2	19	8.0	-0.43
Bopha	7 August 2006	992	1	4	1.5	-0.48
Shanshan	14 September 2006	940	2	7	3.0	-0.45
Wutip	8 August 2007	992	1	5	2.2	-0.41
Sepat	16 August 2007	925	3	23	8.5	-0.52
Krosa	4 October 2007	940	3	35	12.5	-0.40
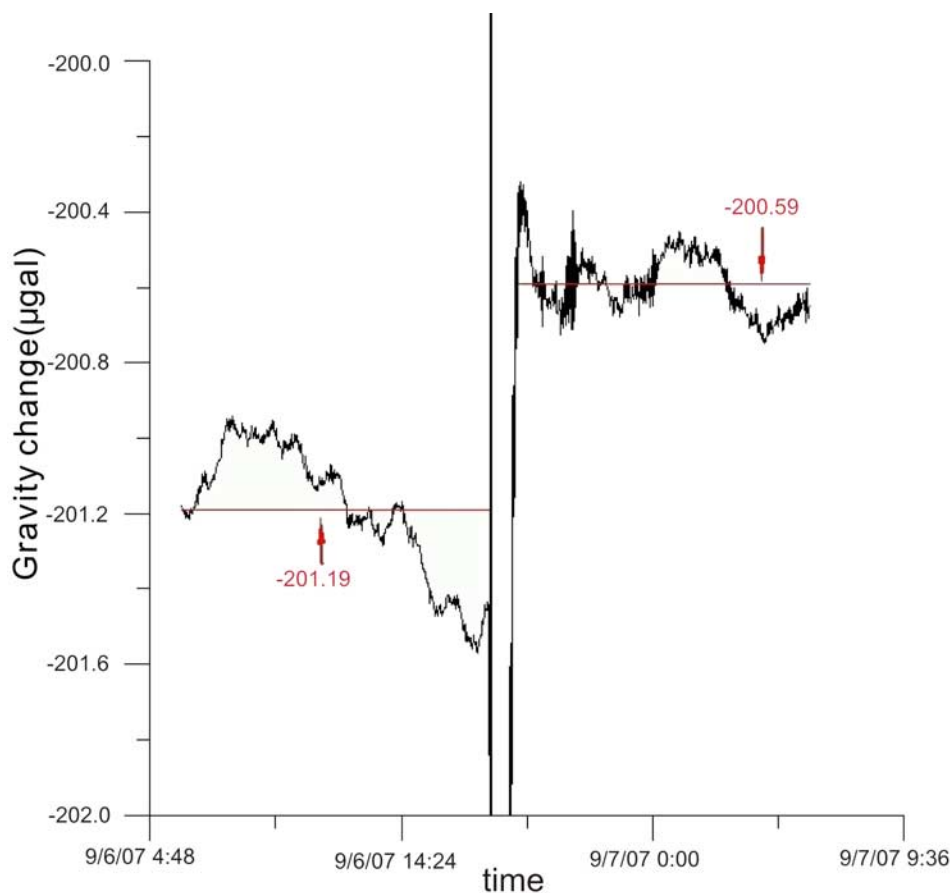
Figure 9. Coseismic gravity change, given as a jump (step function) in the SG gravity records at HS, due to the earthquake on 6 September 2007.

longitude = 122.25°, some 155 km from HS. The gravity change due to the coseismic and postseismic deformations was theoretically studied [e.g., *Wang et al.*, 2006; *Fu and Sun*, 2008]. Although we must carefully check the instrumental instability as a possible source to make the gravity offset shown in Table 8 by comparing the observed offsets to the amplitudes and the directions which are expected from the theoretical estimations and the GPS observations carried out at HS and nearby sites to it. However, Table 8 can be used to validate the theoretical models that estimate coseismic and postseismic gravity changes, and therefore help to refine the fault parameters associated with an earthquake. Furthermore, it is noted that cumulative gravity offsets due to earthquakes will be a possible significant source of the secular gravity rate changes at HS.

7. Residual Gravity Change

7.1. Observations and Models

[27] The observed residual gravity changes at HS were obtained from the raw SG gravity records corrected for the effects of the body and ocean tides (section 4). Several sources contribute to the gravity changes at a given gravity station; a summary of all possible sources is given by *Torge* [1989]. One source is atmospheric pressure change, whose gravity effects at short temporal scales have been discussed in section 5. Another source of gravity change is ground-

water. Depending on the spatial scale sought, the groundwater-induced gravity change is often classified into local, regional and global variations. For a precise modeling of the local groundwater effect, the local hydrogeology data must be given. At HS, the basic scenario of the hydrogeological structure is given in Figures 1 and 2, but far more details are needed to account for the hydrology-induced gravity changes. The water table at HS alone cannot fully describe the distribution of groundwater over the Toukeshan formation around HS and over the alluvium north of HS. Furthermore, a soil moisture sensor is deployed right above Tunnel B that houses T48. However, the soil moisture data collected here will not be representative of water distribution in the unsaturated layers around HS. Despite these difficulties, preliminary models to account for the residual gravity changes at HS due to nongeodynamic origin are presented below.

[28] Model 1, atmospheric pressure effect (μGal), is

$$\delta g_b = f_a(P_a - 1013) \qquad (8)$$

where P_a is pressure in hPa, 1013 hPa is the standard atmospheric pressure at HS, and f_a is the gravity-atmosphere admittance. According to the result in section 5, we set $f_a = -0.350 \ \mu$Gal hPa^{-1}.

Table 8. Gravity Shifts due to Earthquakes Around Taiwan at Hsinchu

Date	Distance (km)	Depth (km)	Magnitude of Earthquake	Gravity Shift (μGal)
1 April 2006	214	9	6.2	1.19
15 April 2006	223	17	6.0	−0.17
28 April 2006	109	8	5.2	−0.61
28 July 2006	170	49	6.0	1.01
27 August 2006	197	145	6.0	0.00
12 October 2006	181	44	5.8	−0.13
14 December 2006	120	7	4.8	−1.10
23 December 2006	138	10	5.4	0.48
26 December 2006	296	44	7.0	−0.41
16 January 2007	191	21	5.4	0.10
25 January 2007	226	26	6.2	−0.31
12 May 2007	101	44	4.9	−0.41
23 July 2007	155	31	6.0	−0.41
9 August 2007	201	4	5.9	−1.41
6 September 2007	155	54	6.6	0.60
11 October 2007	92	80	5.2	0.27
17 October 2007	176	42	5.7	0.01
28 November 2007	91	69	5.4	−0.94

Table 9. Amplitudes and Phases of the Annual Gravity Change at Hsinchu From Different Sources

Source	Amplitude (μGal)	Phase (°)
Observation (T48)	6.24	−26.07
Groundwater	5.48	−88.95
Atmosphere	2.98	−135.34
Soil moisture	1.41	−14.04
Polar motion	1.58	−13.98

$H = 1$ m. The minus sign in equation (10) is due to the fact that T48 is housed in a tunnel beneath the unsaturated soil.

[31] Model 4, polar motion effect (μGal), is

$$\delta g_p = 1.164 \times 10^8 \omega^2 R \sin 2\varphi (x_p \cos \lambda - y_p \sin \lambda) \qquad (11)$$

where ϕ, λ are latitude and longitude and x_p, y_p are polar motion components in radian, which are available from the International Earth Rotation Service (IERS, http://www.iers.org).

[32] Figure 10 compares the observed (by T48) residual gravity changes and the modeled values at HS. Conclusions on the nonlinear gravity changes based on Figure 10 are given below.

[33] 1. At the time scales of hours to days, the largest contribution to the observed residual gravity change is from the atmospheric pressure change. In fact, the analysis in section 5 shows that the correlations between residual gravity change and atmospheric pressure change at such short time scales are more than 90% in most cases. The episodic changes of gravity due to groundwater have to do with sudden rainfalls. The soil moisture also creates short-period gravity variations, but the pattern of variation is quite irregular. There are no clear short-period gravity variations due to polar motions.

[34] 2. The observed and modeled gravity changes all contain annual variations, but with different amplitudes and phases. Table 9 lists these amplitudes and phases. The amplitude of the groundwater gravity effect is the largest, followed by that of the atmosphere gravity effect. The amplitudes of the soil moisture and polar motion-induced annual gravity change are almost equal, and are 1/4 of the groundwater gravity effect. Seasonally, the modeled gravity changes due to atmosphere and groundwater lead the observed residual gravity by 110 and 63 days, while the modeled gravity changes due to soil moisture and polar motion lag behind the observed ones by about 12 days. Disagreements in amplitude and phase between observed gravity change and hydrology-induced gravity change are very common, as shown by *Boy and Hinderer* [2006] and *Neumeyer et al.* [2008] at selected GGP stations. In the case of HS, exactly how and how long the aquifers under the alluvium (Figure 1) are filled and drained are not clear, and these uncertainties contribute to the disagreement between the observed and groundwater-induced gravity changes.

[35] 3. Clearly the models in equations (8)–(11) have deficiencies, e.g., the 63-day phase difference between the observed and groundwater-induced gravity changes. On the other hand, the SG and FG5 observed gravity changes may be used to investigate such problems as flow of

[29] Model 2, groundwater effect (μGal), is

$$\delta g_w = 0.42 P \delta H \qquad (9)$$

where P is the porosity of soil in percentage and δH is groundwater level variation in m. We adopt $P = 10\%$ as the optimal porosity for the Toukeshan formation (section 2).

[30] Model 3, soil moisture effect (μGal), is

$$\delta g_s = -0.42 H \delta P \qquad (10)$$

where H is the depth of unsaturated soil layer and δP is the recorded soil moisture change in percentage. Here we adopt
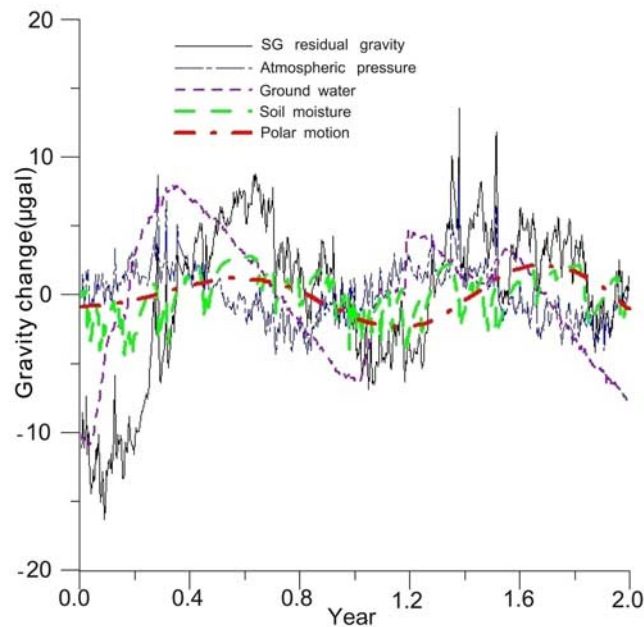

Figure 10. Observed residual gravity changes (by T48, without the body tide and ocean tide gravity effects) and modeled gravity changes at HS. The time starts from March 2006.

Table 10. Modeled and FG5-Observed Rates of Gravity Change at Hsinchu

Source	Rate (μGal a^{-1})
Atmosphere	−1.3
Groundwater	3.8
Soil moisture	0.5
Polar motion	0.4
Free-air motion of site	−0.1
Total	3.3
FG5 observations	2.2

groundwater and small-scale hydrological process [see, e.g., *Jacob et al.*, 2008; *Naujoks et al.*, 2008].

7.2. Rate of Gravity Change at HS

[36] As shown in section 3.2, the absolute and T48 gravity records all show a long-term trend of gravity change at HS. The origins of the trend are now interpreted using the modeled gravity changes given in section 7.1, plus the vertical displacement given in section 2. The rates of the modeled gravity changes are listed in Table 10. The total rate from these models is 3.3 ± 0.8 μGal a^{-1}, compared to 2.2 ± 0.7 μGal a^{-1} from the absolute gravimeter measurements (section 3.2). Therefore, the modeled rates cannot fully account for the observed rate of gravity change. One source of the gravity change not accounted for in Table 10 at HS is earthquakes around Taiwan. For example, the earthquake occurring on 6 September 2007 created a gravity offset of 0.6 μGal, which contributes a rate of 0.3 μGal a^{-1} to the total rate at HS over 2 years (section 6). Other small earthquakes will also create gravity changes that eventually add to the rate of gravity change at HS. Gravity change due to sea level rise will also contribute to the rate of gravity change recorded at HS. An example of gravity change due to sea level rise over the Baltic Sea is given by *Virtanen and Makinen* [2003]. At the global scale, a rising rate of 3.1 mm a^{-1} in sea level, as estimated from TOPEX/Poseidon and Jason-1 satellite altimeter data [*Nerem et al.*, 2006], will lead to a rate of 0.2 μGal a^{-1} in gravity based on a simple Bouguer model for the effect of oceanic water mass.

8. Conclusions

[37] This paper summarizes the findings from the observations of a superconducting gravimeter (T48), three FG5 absolute gravimeters (serials 224, 228, and 231) and a regional GPS network around HS. The main purpose of this work is to show some of T48's critical parameters and its potential applications to such studies as SET, OTGE, typhoon and earthquake. The area north of HS is a groundwater-rich alluvium that introduces gravity variation at HS. A vertical site motion of 0.5 ± 0.3 mm a^{-1} at HS was found and is not directly related to the movement of the Hsinchu Fault. Using the parallel FG5 and T48 observations, the calibration factor and the drifting rate of T48 were found to be −75.96 ± 0.07 μGal V^{-1} and 0.2 ± 0.7 μGal a^{-1}, respectively. The observed drifting rate of T48 is smaller than the nominal drift of few μGal a^{-1} reported by the SG manufacturer. The relative differences between the gravimetric amplitude factors determined with T48 (corrected by NAO.99b) and the model factors of *Dehant et al.* [1999] range from 0.05 to 3.93%. The OTGE model amplitudes

and phases from the NAO.99b tide model agree the best with the observations of T48. The Newtonian part contributes a significant portion to OTGE (about 20% for M_2 at HS) at an oceanside SG station such as HS. A density distribution model of atmospheric pressure change based on an exponential function predicts the gravity-atmosphere admittances that agree well with the observations. The gravity-atmosphere admittances during typhoons are 30% larger than the mean.

[38] The residual gravity from T48 shows a distinct annual cycle and a linear trend. Four models of temporal gravity changes are used to explain the SG residual gravity, but there exist a significant discrepancy between the observations of T48 and the model values. Seasonally, the groundwater-induced gravity change leads the SG residual gravity by 63 days. The phases of the annual cycles from other sources deviate from that of the SG residual gravity by tens of days to a few months. Both typhoons and earthquakes around Taiwan created large gravity variations at HS. The SG records at HS are able to detect coseismic gravity changes around Taiwan, and the example given in this paper serves as the beginning of the SG earthquake research using the SG data at HS. In summary, with the necessary information presented in this paper, the SG (T48) at HS has delivered data that meet the quality standard and are ready to be used in a number of geodetic and geophysical problems.

References

Beutler, G., et al. (2007), *Bernese GPS Software Version 5.0*, Astron. Inst., Univ. of Bern, Bern, Switzerland.

Boy, J. P., and J. Hinderer (2006), Study of the seasonal gravity signal in superconducting gravimeter data, *J. Geodyn.*, 41, 227–233, doi:10.1016/j.jog.2005.08.035.

Boy, J. P., M. Llubes, J. Hinderer, and N. Florsch (2003), A comparison of tidal ocean loading models using superconducting gravimeter data, *J. Geophys. Res.*, 108(B4), 2193, doi:10.1029/2002JB002050.

Boy, J. P., M. Llubes, R. Ray, J. Hinderer, N. Florsch, S. Rosat, F. Lyard, and T. Letellier (2004), Non-linear oceanic tides observed by superconducting gravimeters in Europe, *J. Geodyn.*, 38, 391–405, doi:10.1016/j.jog.2004.07.017.

Chou, C. B., C. Y. Huang, H. P. Huang, K. H. Wang, and T. C. Yeh (2008), The analysis of typhoon structures using advanced microwave sounding unit data and its application to prediction, *J. Appl. Meteorol. Climatol.*, 47, 1476–1492, doi:10.1175/2007JAMC1577.1.

Dehant, V., P. Defraigne, and J. M. Wahr (1999), Tides for a convective Earth, *J. Geophys. Res.*, 104, 1035–1058, doi:10.1029/1998JB900051.

Dziewonski, A. D., and D. L. Anderson (1981), Preliminary reference Earth model, *Phys. Earth Planet. Inter.*, 25, 297–356, doi:10.1016/0031-9201(81)90046-7.

Eanes, R., and S. Bettadpur (1996), The CSR3.0 global ocean tide model: Diurnal and semi-diurnal ocean tides from TOPEX/POSEIDON altimetry, *Tech Rep. CRS-TM-96–05*, Univ. of Tex. Cent. for Space Res., Austin.

Farrell, W. E. (1972), Deformation of the Earth by surface loads, *Rev. Geophys.*, 10, 761–797, doi:10.1029/RG010i003p00761.

Forsberg, R., M. G. Sideris, and C. K. Shum (2005), The gravity field and GGOS, *J. Geodyn.*, 40, 387–393, doi:10.1016/j.jog.2005.06.014.

Francis, O., T. M. Niebauer, G. Sasagawa, F. Klopping, and J. Gschwind (1998), Calibration of a superconducting gravimeter by comparison with an absolute gravimeter FG5 in Boulder, *Geophys. Res. Lett.*, 25, 1075–1078, doi:10.1029/98GL00712.

Fu, G. Y., and W. K. Sun (2008), Surface coseismic gravity changes caused by dislocations in a 3-D heterogeneous Earth, *Geophys. J. Int.*, *172*, 479–503, doi:10.1111/j.1365-246X.2007.03684.x.

Heiskanen, W. A., and H. Moritz (1985), *Physical Geodesy*, reprint, Tech. Univ. Graz, Austria.

Hinderer, J., and D. Crossley (2004), Scientific achievements from the first phase (1997–2003) of the Global Geodynamics Project using a worldwide network of superconducting gravimeters, *J. Geodyn.*, *38*, 237–262, doi:10.1016/j.jog.2004.07.019.

Huang, J. F., C. Hwang, and S. Jan (2008), Modeling gravity effect of ocean tidal loading around Taiwan: Accuracy assessment using FG5 and superconducting gravity data, *Eos Trans. AGU*, *89*(23), West. Pac. Geophys. Meet. Suppl., Astract G41A-02.

Imanishi, Y., T. Higashi, and Y. Fukuda (2002), Calibration of the superconducting gravimeter T011 by parallel observation with the absolute gravimeter FG5 #210: A Bayesian approach, *Geophys. J. Int.*, *151*, 867–878, doi:10.1046/j.1365-246X.2002.01806.x.

Imanishi, Y., T. Sato, T. Higashi, W. K. Sun, and S. Okubo (2004), A network of superconducting gravimeters detects submicroGal coseismic gravity changes, *Science*, *306*, 476–478, doi:10.1126/science.1101875.

Jacob, T., R. Bayer, J. Chery, H. Jourde, N. Le Moigne, J. P. Boy, J. Hinderer, B. Luck, and P. Brunet (2008), Absolute gravimetry monitoring of water storage variation in a karst aquifer on the larzac plateau (southern France), *J. Hydrol.*, *359*, 105–117, doi:10.1016/j.jhydrol.2008.06.020.

Jan, S., C. S. Chern, J. Wang, and S. Y. Chao (2004), The anomalous amplification of M_2 tide in the Taiwan Strait, *Geophys. Res. Lett.*, *31*, L07308, doi:10.1029/2003GL019373.

Johnson, K. M., P. SeGall, and S. B. Yu (2005), A viscoelastic earthquake cycle model for Taiwan, *J. Geophys. Res.*, *110*, B10404, doi:10.1029/2004JB003516.

Khan, S. A., and J. L. Høyer (2004), Shallow-water loading tides in Japan from superconducting gravimetry, *J. Geod.*, *78*, 245–250, doi:10.1007/s00190-003-0391-4.

Li, Q. Q., Y. H. Duan, H. Yu, and G. Fu (2008), A high-resolution simulation of Typhoon Rananim (2004) with MM5: Part I. Model verification, inner-core shear, and asymmetric convection, *Mon. Weather Rev.*, *136*, 2488–2506, doi:10.1175/2007MWR2159.1.

Llubes, M., N. Florsch, J. Hinderer, L. Longuevergne, and M. Amalvict (2004), Local hydrology, the Global Geodynamics Project and CHAMP/GRACE perspective: Some case studies, *J. Geodyn.*, *38*, 355–374, doi:10.1016/j.jog.2004.07.015.

Lyard, F., F. Lefevre, T. Letellier, and O. Francis (2006), Modeling the global ocean tides: Modern insights from FES2004, *Ocean Dyn.*, *56*, 394–415, doi:10.1007/s10236-006-0086-x.

Lysaker, D. I., K. Breili, and B. R. Pettersen (2008), The gravitational effect of ocean tide loading at high latitude coastal stations in Norway, *J. Geod.*, *82*, 569–583, doi:10.1007/s00190-007-0207-4.

Matsumoto, K., T. Takanezawa, and M. Ooe (2000), Ocean tide models developed by assimilating TOPEX/POSIDON altimeter data into hydrodynamical model: A global model and a regional model around Japan, *J. Oceanogr.*, *56*, 567–581, doi:10.1023/A:1011157212596.

Matsumoto, K., T. Sato, H. Fujimoto, Y. Tamura, M. Nishino, R. Hino, and T. Higashi (2006), Ocean bottom pressure observation off Sanriku and comparison with ocean tide models, altimetry, and barotropic signals from ocean models, *Geophys. Res. Lett.*, *33*, L16602, doi:10.1029/2006GL026706.

Naujoks, M., A. Weise, C. Kroner, and T. Jahr (2008), Detection of small hydrological variations in gravity by repeated observations with relative gravimeters, *J. Geod.*, *82*, 543–553, doi:10.1007/s00190-007-0202-9.

Nerem, R. S., E. Leuliette, and A. Cazenave (2006), Present-day sea-level change: A review, *C. R. Geosci.*, *338*, 1077–1083, doi:10.1016/j.crte.2006.09.001.

Neumeyer, J., J. Hagedoorn, J. Leitloff, and T. Schmidt (2004), Gravity reduction with three-dimensional atmospheric pressure data for precise ground gravity measurements, *J. Geodyn.*, *38*, 437–450, doi:10.1016/j.jog.2004.07.006.

Neumeyer, J., F. Barthelmes, C. Kroner, S. Petrovic, R. Schmidt, H. Virtanen, and H. Wilmes (2008), Analysis of gravity field variations derived from superconducting gravimeter recordings, the GRACE satellite and hydrological models at selected European sites, *Earth Planets Space*, *60*, 505–518.

Ooe, M., and H. Hanada (1982), Physical simulations of effects of the atmospheric pressure and the ground water upon gravitational acceleration and crustal deformation, *Publ. Int. Lat. Obs. Mizusawa*, *21*, 6–14.

Penna, T. N., M. A. King, and M. P. Stewart (2007), GPS height time series: Short-period origins of spurious long-period signals, *J. Geophys. Res.*, *112*, B02402, doi:10.1029/2005JB004047.

Riccardi, U., J. Hinderer, and J. P. Boy (2007), On the efficiency of barometric arrays to improve the reduction of atmospheric effects on gravity, *Phys. Earth Planet. Inter.*, *161*, 224–242, doi:10.1016/j.pepi.2007.02.007.

Sato, T., and H. Hanada (1984), A program for the computation of oceanic tidal loading effects "GOTIC,", *Publ. Int. Lat. Obs. Mizusawa*, *18*, 29–47.

Shiomi, S. (2006), Geophysical test of the universality of free-fall, *Phys. Rev. D*, *74*, 027101, doi:10.1103/PhysRevD.74.027101.

Tamura, Y., T. Sato, M. Ooe, and M. Ishiguro (1991), A procedure for tidal analysis with a Bayesian information criterion, *Geophys. J. Int.*, *104*, 507–516, doi:10.1111/j.1365-246X.1991.tb05697.x.

Tamura, Y., T. Sato, Y. Fukuda, and T. Higashi (2004), Scale factor calibration of a superconducting gravimeter at Esashi Station, Japan, using absolute gravity measurements, *J. Geod.*, *78*, 481–488, doi:10.1007/s00190-004-0415-0.

Torge, W. (1989), *Gravimetry*, De Gruyter, Berlin.

Virtanen, H., and J. Makinen (2003), The effect of the Baltic sea level on gravity at the Metsahovi station, *J. Geodyn.*, *35*, 553–565, doi:10.1016/S0264-3707(03)00014-0.

Wahr, J. (1981), Body tides on an elliptical, rotating, elastic and oceanless Earth, *Geophys. J. R. Astron. Soc.*, *64*, 677–704.

Wang, R. J., F. Lorenzo-Martín, and F. Roth (2006), PSGRN/PSCMP: A new code for calculating co- and post-seismic deformation, geoid and gravity changes based on the viscoelastic-gravitational dislocation theory, *Comput. Geosci.*, *32*, 527–541, doi:10.1016/j.cageo.2005.08.006.

Wenzel, H. G. (1996), The nanoGal software: Earth tide processing package ETERNA 3.30, *Bull. Inf. Marées Terr.*, *124*, 9425–9439.

Wunsch, C., and D. Stammer (1997), Atmospheric loading and the oceanic "inverted barometer" effect, *Rev. Geophys.*, *35*, 79–107, doi:10.1029/96RG03037.

————————

C.-C. Cheng, J.-F. Huang, C. Hwang, and R. Kao, Department of Civil Engineering, National Chiao Tung University, 1001 Ta Hsueh Road, Hsinchu 300, Taiwan. (cheinway@mail.nctu.edu.tw)

C.-W. Lee, Dimensional Measurement Laboratory, Measurement Standards and Technology Division, CMS, ITRI, 321 Kuang Fu Road., Section 2, Hsinchu 300, Taiwan.

T. Sato, Research Center for Prediction of Earthquakes and Volcanic Eruptions, Tohoku University, 6-6 Aza-Aoba, Aramaki, Aoba-ku, Sendai 980-8578, Japan.